GEOPHYSICS, VOL. 84, NO. 2 (MARCH-APRIL 2019); P. N29–N40, 14 FIGS.
10.1190/GEO2018-0128.1

Check for updates

Downloaded 03/14/19 to 138.67.129.23. Redistribution subject to SEG license or copyright; see Terms of Use at http://library.seg.org/

Appraising structural interpretations using seismic data — Theoretical elements

Modeste Irakarama[1], Paul Cupillard[1], Guillaume Caumon[1], Paul Sava[2], and Jonathan Edwards[1]

ABSTRACT

Structural interpretation of seismic images can be highly subjective, especially in complex geologic settings. A single seismic image will often support multiple geologically valid interpretations. However, it is usually difficult to determine which of those interpretations are more likely than others. We have referred to this problem as structural model appraisal. We have developed the use of misfit functions to rank and appraise multiple interpretations of a given seismic image. Given a set of possible interpretations, we compute synthetic data for each structural interpretation, and then we compare these synthetic data against observed seismic data; this allows us to assign a data-misfit value to each structural interpretation. Our aim is to find data-misfit functions that enable a ranking of interpretations. To do so, we formalize the problem of appraising structural interpretations using seismic data and we derive a set of conditions to be satisfied by the data-misfit function for a successful appraisal. We investigate vertical seismic profiling (VSP) and surface seismic configurations. An application of the proposed method to a realistic synthetic model shows promising results for appraising structural interpretations using VSP data, provided that the target region is well-illuminated. However, we find appraising structural interpretations using surface seismic data to be more challenging, mainly due to the difficulty of computing phase-shift data misfits.

INTRODUCTION

Uncertainties in structural interpretations of seismic images have been of interest to geoscientists for a long time. Earlier studies were mainly focused on migration velocity errors and seismic resolution; some examples can be found in Hajnal and Sereda (1981) and Beylkin et al. (1985). Structural uncertainties propagated from velocity errors usually translate to subtle displacement or flexing of horizons and faults away from the reference position of those horizons and faults (Thore and Haas, 1996; Bube et al., 2004; Pon and Lines, 2005; Fomel and Landa, 2014). By the reference position of a given horizon or fault, one often means the position obtained from the tomographic velocity model (e.g., Messud et al., 2017). Geologic realizations obtained by such perturbations of a reference structural model often underestimate structural uncertainties because interpretation uncertainties are not taken into account. Interpretation uncertainties arise where reflectors cannot be tracked deterministically; this can be a result of an inaccurate imaging velocity model (Li et al., 2015), poor illumination, and/or poor resolution (Lecomte et al., 2016). In these situations, multiple geologically possible structural models can be interpreted from the same seismic image (Bond et al., 2007; Bond, 2015; Alcalde et al., 2017).

Generating multiple structural models from a single data set was one of the earliest methods proposed to evaluate structural uncertainties in geomodeling (Thore et al., 2002). This method opened ways to new challenges, two of which are

1) Sampling structural uncertainties: This is essentially a structural modeling problem (Abrahamsen, 1993; Lecour et al., 2001; Holden et al., 2003; Wellmann et al., 2010, 2014; Cherpeau and Caumon, 2015; Julio et al., 2015). In particular, how can we generate multiple structural models respecting the uncertainty bounds and the geologic rules efficiently?
2) Appraising structural models: This usually amounts to evaluating the model's response for some observed physical phenomenon. In most studies on structural model appraisal, the physical

Manuscript received by the Editor 12 February 2018; revised manuscript received 10 September 2018; published online 28 February 2019.
[1]Université de Lorraine, CNRS, GeoRessources Lab., 2 rue du Doyen Marcel Roubault, Vandoeuvre-lès-Nancy, Nancy 54518, France. E-mail: modeste.irakarama@univ-lorraine.fr; paul.cupillard@univ-lorraine.fr; guillaume.caumon@univ-lorraine.fr; jonathan.edwards@univ-lorraine.fr.
[2]Colorado School of Mines, 1500 Illinois St., Golden, Colorado 80401, USA. E-mail: psava@mines.edu.
© 2019 Society of Exploration Geophysicists. All rights reserved.

Downloaded 03/14/19 to 138.67.129.23. Redistribution subject to SEG license or copyright; see Terms of Use at http://library.seg.org/

phenomenon that has been used to evaluate the model is fluid flow (Suzuki et al., 2008; Cherpeau et al., 2012). Potential fields (gravity and magnetic) have also been used to validate model scenarios (Foss et al., 2008; Fullagar et al., 2008).

With standard geomodeling workflows, we are able to generate multiple geologic scenarios from a seismic image, but we rarely go back to check if these models are consistent with the initial data; doing so would be a way to reduce structural uncertainty. Here, initial data refer to the recorded premigrated seismic traces. An interesting approach proposed by Lecomte et al. (2003) to address this issue is to generate synthetic seismic images from different geologic scenarios and compare them with the initial seismic image; a similar approach was adopted by Lallier et al. (2012). A major challenge of this approach is that it is not clear how to objectively compare seismic images. An alternative way for reducing interpretation uncertainties in structural modeling is to use "data-driven" interpretation approaches. Here, data-driven interpretation includes all the methods that have been proposed to automatically track horizons and faults and to build a relative-geologic-time function from a seismic image (Stark, 2004; Pauget et al., 2009; Wu and Hale, 2015; Wu, 2017). Data-driven techniques, however, require good-quality seismic data (Hoyes and Cheret, 2011); where the geology is complex or lacks reflectivity contrasts, manual interpretation is still necessary.

In this paper, we aim to reduce interpretation uncertainties by appraising structural interpretations using seismic data. Our approach is conceptually similar to that proposed by Lecomte et al. (2003): We generate synthetic data from a set of candidate geologic models, and then we compare the synthetic data against the observed data. The candidate geologic models are obtained from different interpretations of the same seismic image. There are two main differences between the method proposed here and the method proposed by Lecomte et al. (2003). First, we compare initial premigrated data instead of seismic images; second, we propose a quantitative comparison instead of a qualitative comparison. The objective of this paper is to investigate how exactly we should compare synthetic data against observed data. We mainly focus on theoretical aspects of the problem and defer the more practical issues for further investigations.

In what follows, we introduce the problem of appraising structural interpretations using seismic data and we propose a mathematical formulation to describe the process. We then propose some strategies to build a velocity model with structural discontinuities from a structural interpretation and a (smooth) migration velocity model; the resulting velocity model with structural discontinuities is then used to generate synthetic data for the given structural interpretation. Finally, we propose a workflow to design data misfit functions to evaluate and rank the different structural interpretations. The proposed method is then applied on a realistic synthetic vertical seismic profiling (VSP) case.

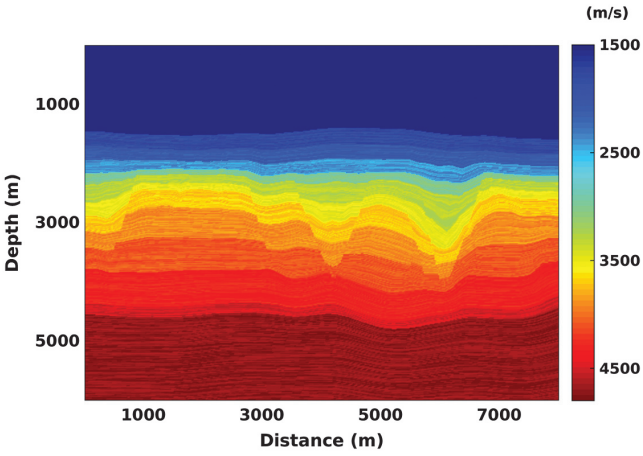


Figure 1. The reference velocity model. It is derived from the sandbox model of Colletta et al. (1991).

THE STRUCTURAL INTERPRETATION APPRAISAL PROBLEM

We use the model in Figure 1 to illustrate an example of interpretation uncertainty. The model was built by assigning constant velocity values in each major layer of the sandbox model of Colletta et al. (1991). Additional thin-layering structures were added inside each major layer to generate more realistic synthetic seismic data (Landa and Thore, 2007). The resulting velocity model was then used to simulate "observed" seismic data using an acoustic, constant density, staggered finite-difference scheme (Virieux, 1984) with perfectly matched absorbing boundaries (Collino and Tsogka, 2001). All subsequent seismic modeling mentioned in this paper were performed with the same code. The reference velocity model in Figure 1 was also used to obtain the migration velocity model in Figure 2a by Gaussian smoothing of the slowness; this migration

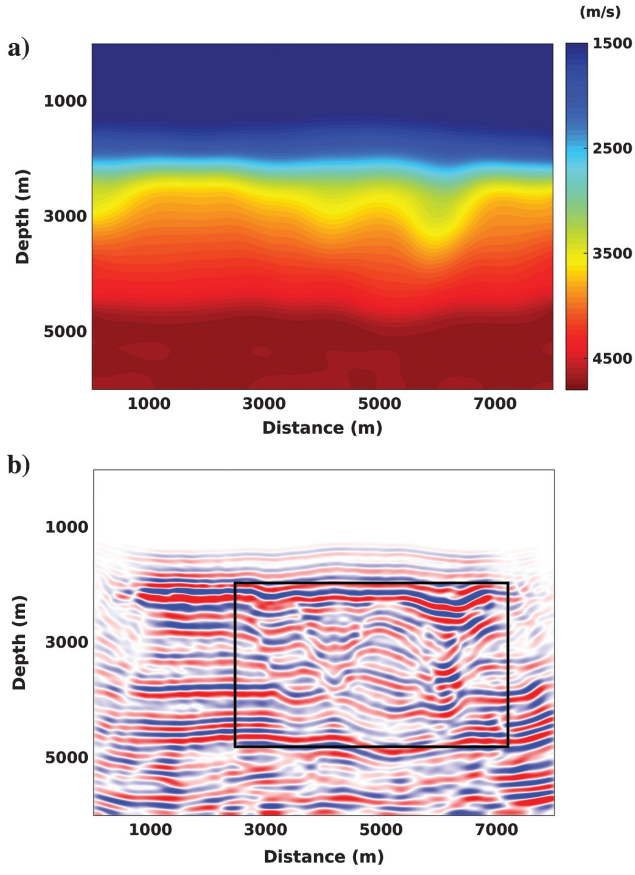


Figure 2. (a) Migration velocity model obtained by smoothing the slowness of the reference model in Figure 1. (b) Depth-migrated image (KDM) of data computed from the reference model. The black box is the region of interest.

velocity model was then used to migrate the observed data to obtain the seismic image in Figure 2b using Kirchhoff depth migration (KDM) (e.g., Etgen et al., 2009).

Figure 3a and 3b shows two different structural interpretations of the seismic image in Figure 2b from two different interpreters. Both interpretations are geologically possible, but they are different in some regions. Assuming that one is more accurate than the other in the regions where they differ, can we use seismic data to determine which of the two models is more accurate in those regions? To answer this question, we rely on macrolayered velocity models. Macrolayered velocity models are defined as velocity models with discontinuities from structural models and velocity values from the migration model (e.g., Figure 3c and 3d). The migration velocity model is assumed to be kinematically accurate throughout this paper. We use these macrolayered velocity models to compute synthetic data, which are compared against the observed data to appraise the different geologic scenarios.

Structural interpretations are typically segments or curves picked by interpreters along structural discontinuities on a seismic image. A structural model is a set of consistent structural surfaces, such as horizons and faults, that represent a geologic model (Caumon et al., 2009) (e.g., Figure 3a and 3b). In this paper, structural models are built from structural interpretations and there is a one-to-one relation from structural interpretations to structural models. Therefore, appraising structural interpretations is synonymous with appraising structural models herein. The relation from structural models to macrolayered velocity models is assumed to be one to one as well.

Let us define a model misfit as a number that quantifies the mismatch between the reference structural model and a candidate structural model. The reference structural model is the "true" structural model; it is unknown in practice. However, for the sake of argument, we assume the reference model to be known for now. Let us also assume that we can determine this model-misfit value for each model in a given set of candidate structural models. Furthermore, we assume that different models will have different model-misfit values, allowing us to rank those models from the best model to the worst model. This ranking of structural models using model-misfit values will be referred to as model-space ranking of structural models. Objects in the model space are structural interpretations, or alternatively structural models. We also define a data misfit as a number that quantifies the mismatch between observed data and the synthetic data generated from candidate structural models. Data-misfit values will allow us to rank structural interpretations in the data space; we refer to this as data-space ranking. The data space here refers to the premigration domain; i.e., objects in the data-space are seismic traces. We assume that the observed data are the wave equation's response of the reference model (true earth) subjected to some acquisition geometry, just like synthetic data are the wave equation's response of a given candidate (synthetic) model. If the ranking in the data space is the same as the ranking in the model

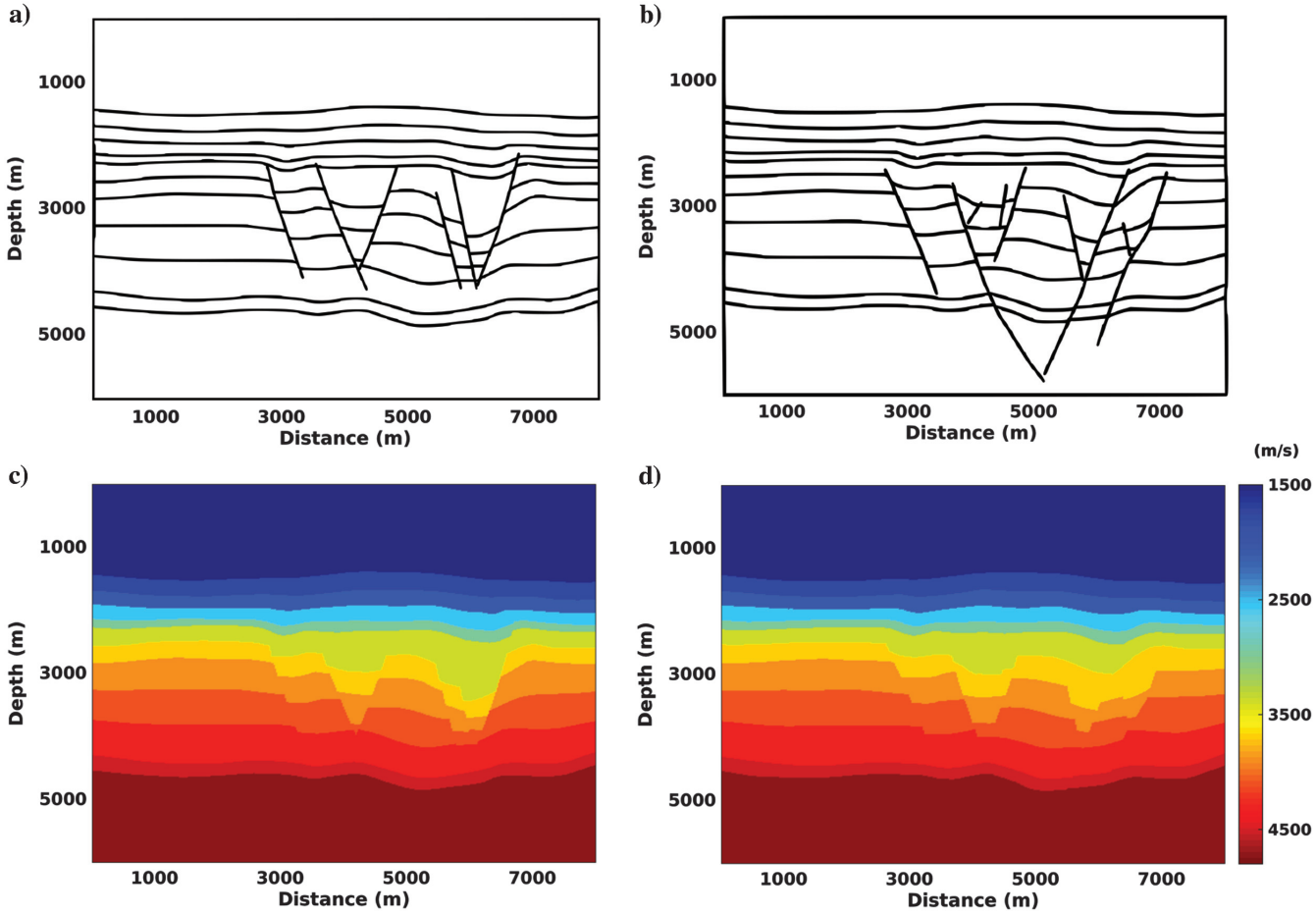


Figure 3. (a and b) Two possible structural interpretations/models of Figure 2b from different interpreters. (c and d) Macrolayered velocity models built from the migration velocity model and the structural models.

Downloaded 03/14/19 to 138.67.129.23. Redistribution subject to SEG license or copyright; see Terms of Use at http://library.seg.org/

Downloaded 03/14/19 to 138.67.129.23. Redistribution subject to SEG license or copyright; see Terms of Use at http://library.seg.org/

space, then we do not need to know the reference model to determine which among our candidate models are more probable than others. For this reasoning to be applicable, the following conditions have to be satisfied:

- Different candidate structural models should, overall, have different data-misfit values.
- Data-misfit values should, overall, be rank-correlated to model-space misfit values.

In practice, a pair of different structural models may exhibit similar seismic response at receivers; in this case, the first condition can be satisfied by ignoring one of the models. The second condition means that if we plot model misfits and data misfits on a scatterplot, we should be able to find a monotonic curve that fits the data.

In general, it is straightforward to design data-misfit functions and compute data-misfit values. However, it is much harder to design data misfits that satisfy the conditions mentioned above. The objective of this paper is to investigate what it takes to define data-misfit functions that honor the conditions mentioned above as much as possible and thus run the process with real data, where the reference (true) model truly is unknown.

MATHEMATICAL FORMULATION

Let $\mathbf{M}_i$ denote a candidate structural model (e.g., Figure 3a and 3b), the index i taking different values for different interpretation scenarios. Each structural model $\mathbf{M}_i$ can be used, together with the migration velocity model, to build a macrolayered velocity model, also denoted by $\mathbf{M}_i$. Examples of macrolayered velocity models will be presented in the next section (see also Figure 3c and 3d).

Let us introduce the model-space misfit function $\Phi^m_{i,j}$ that measures the difference between two structural models $\mathbf{M}_i$ and $\mathbf{M}_j$ and denote the mismatch between the reference model and a candidate model $\mathbf{M}_i$ as $\Phi^m_i = \Phi^m_{i,\text{ref}}$. Similarly, we introduce a data-space misfit $\Phi^d_{i,j}$ that measures the difference between data computed in two macrolayered models $\mathbf{M}_i$ and $\mathbf{M}_j$, and we denote the mismatch between data computed in the macrolayered model $\mathbf{M}_i$ and the observed (reference) data as $\Phi^d_i = \Phi^d_{i,\text{ref}}$. Two models $\mathbf{M}_i$ and $\mathbf{M}_j$ are said to be data-different if $|\Phi^d_i - \Phi^d_j| > \epsilon$, for some "small" user-defined threshold $\epsilon > 0$.

Let $\mathcal{M}$ be a set of data-different structural models. If Φ^d_i and Φ^m_i are perfectly rank-correlated for all models in $\mathcal{M}$, then ranking models in $\mathcal{M}$ using Φ^d_i is the same as ranking models in $\mathcal{M}$ using Φ^m_i. In that case, by definition, the structural models in $\mathcal{M}$ can be appraised (i.e., ranked) using seismic data. Therefore, given a set of macrolayered velocity models $\mathcal{M}$, we consider the problem of appraising structural models using seismic data to be solvable in $\mathcal{M}$ if the following conditions are satisfied:

- condition 1: $|\Phi^d_j - \Phi^d_i| > \epsilon$ when $i \neq j$
- condition 2: $\infty > \frac{\Phi^d_j - \Phi^d_i}{\Phi^m_j - \Phi^m_i} > 0$ when $i \neq j$.

Given a set of random structural models $\mathcal{R}$, we can build a set of data-different structural models $\mathcal{M}$ by progressively moving each model $\mathbf{M}_i$ from $\mathcal{R}$ to $\mathcal{M}$, when $\mathbf{M}_i$ is data different from all the models already in $\mathcal{M}$. Therefore, condition 1 can be satisfied in practice. We focus on condition 2 hereafter. Let us define $\Phi^d_i(\Omega)$ and $\Phi^m_i(\Omega)$, respectively, as the data-space and model-space misfit values corresponding to a specific region Ω in the candidate model $\mathbf{M}_i$. The reason for localizing misfits in space will be justified later. In that case, two necessary conditions, although not sufficient, for (the localized version of) condition 2 to be satisfied are

- condition 3: a change of $\Phi^d_i(\Omega) \Rightarrow$ a change of $\Phi^m_i(\Omega)$
- condition 4: a change of $\Phi^m_i(\Omega) \Rightarrow$ a change of $\Phi^d_i(\Omega)$.

The symbol $\Rightarrow$ stands for "implies." Furthermore, suppose that Φ^m satisfies the following condition:

- condition 5: a change of $\Phi^m_i(\Omega) \Leftrightarrow$ a change of the structural model $\mathbf{M}_i$ in Ω.

Then, conditions 3 and 4 become:

- condition 6: a change of $\Phi^d_i(\Omega) \Rightarrow$ a change of the structural model $\mathbf{M}_i$ in Ω
- condition 7: a change of the structural model $\mathbf{M}_i$ in $\Omega \Rightarrow$ a change of $\Phi^d_i(\Omega)$.

At this point, we have transformed the problem of appraising structural models using seismic data to that of satisfying one condition on Φ^m (condition 5) and three conditions on Φ^d (conditions 1, 6, and 7). The conditions imposed on Φ^d can be checked in practice because they do not depend on the (unknown) reference model. Note that condition 2 implies that we assume the relation between the model and data to be weakly nonlinear; i.e., we assume the perturbations in conditions 3 and 4 to be small. In other words, we assume, to some extent, that all the candidate structural models are close to the (unknown) reference model.

Our goal will be to design Φ^d such that conditions 6 and 7 are honored as much as possible. We will argue that for VSP data misfits, condition 7 is relatively easy to satisfy, whereas condition 6 is practically impossible to satisfy in general. As for surface seismic data-misfit functions, we will argue that if all the candidate macrolayered velocity models are kinematically equivalent to the migration velocity model, itself assumed to be kinematically accurate, conditions 6 and 7 can be satisfied in theory for stratified (i.e., layered) models; however, it remains challenging to design and compute misfit function satisfying these conditions. These difficulties make the ideal condition 2 too strict in practice; we replace it with the less ambitious condition

- condition 8: Φ^d is statistically rank-correlated with Φ^m.

Condition 2 means that the rank correlation coefficient of the variables Φ^m and Φ^d is 1, whereas condition 8 means that it is "high enough."

MACROLAYERED VELOCITY MODELS

We propose several options for building macrolayered velocity models from a structural interpretation and a migration model. In this section, we use the illustrative model in Figure 4a as the reference model and the model in Figure 4b as the migration model; the migration model was obtained by smoothing the slowness of the reference model.

Block macrolayered velocity model

The first type of macrolayered model we propose is obtained by averaging migration slowness values (Figure 4b) in each layer of a structural model. Averaging slowness values preserves traveltimes,

Downloaded 03/14/19 to 138.67.129.23. Redistribution subject to SEG license or copyright; see Terms of Use at http://library.seg.org/

as opposed to averaging velocities. The velocity of the ith layer is therefore given by

$$v_i = \text{mean}\left[\left\{\frac{1}{\mathbf{M}^{\text{mig}}(\mathbf{x})}\middle|\mathbf{x} \text{ in layer } i\right\}\right]. \quad (1)$$

This results in a block velocity model, denoted $\mathbf{M}^b$ hereafter, as illustrated in Figure 5a. Figure 5b shows velocity model residuals obtained by subtracting the reference model from the block macrolayered model. Well-log information, when available, can also be used to constrain velocity values assigned in each layer of block macrolayered models. Block macrolayered velocity models are not, in general, kinematically equivalent to the migration velocity model.

Wire macrolayered velocity model

The second type of macrolayered model is the wire velocity model $\mathbf{M}^w$, illustrated in Figure 6. This model is obtained by

$$\mathbf{M}^w(\mathbf{x}) = \mathbf{M}^{\text{mig}}(\mathbf{x}) + \Delta\mathbf{M}^b(\mathbf{x}), \quad (2)$$

where $\Delta\mathbf{M}^b(\mathbf{x})$ denotes the velocity contrast at point $\mathbf{x}$; it is equal to zero everywhere except at block boundaries, where it is equal to the velocity jump between the velocities in adjacent blocks. Wire macrolayered velocity models are kinematically equivalent to the migration velocity model everywhere expect at geologic interfaces.

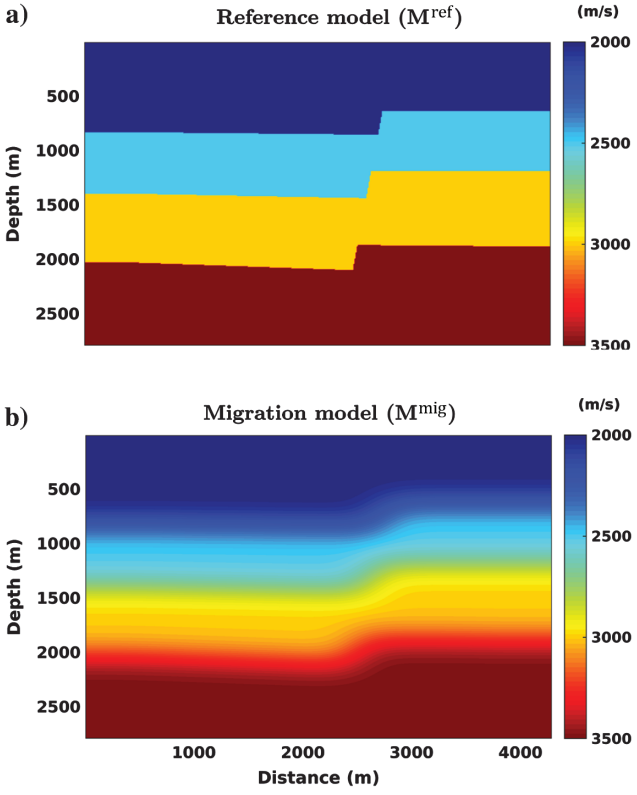


Figure 4. (a) Reference model ($\mathbf{M}^{\text{ref}}$). (b) Migration model ($\mathbf{M}^{\text{mig}}$) obtained by smoothing the slowness of the reference model.

Reflectivity macrolayered velocity model

We also propose the reflectivity velocity model $\mathbf{M}^r$ illustrated in Figure 7 and obtained by

$$\mathbf{M}^r(\mathbf{x}) = \mathbf{M}^{\text{mig}}(\mathbf{x}) + [\mathbf{M}^b(\mathbf{x}) - \bar{\mathbf{M}}^b(\mathbf{x})], \quad (3)$$

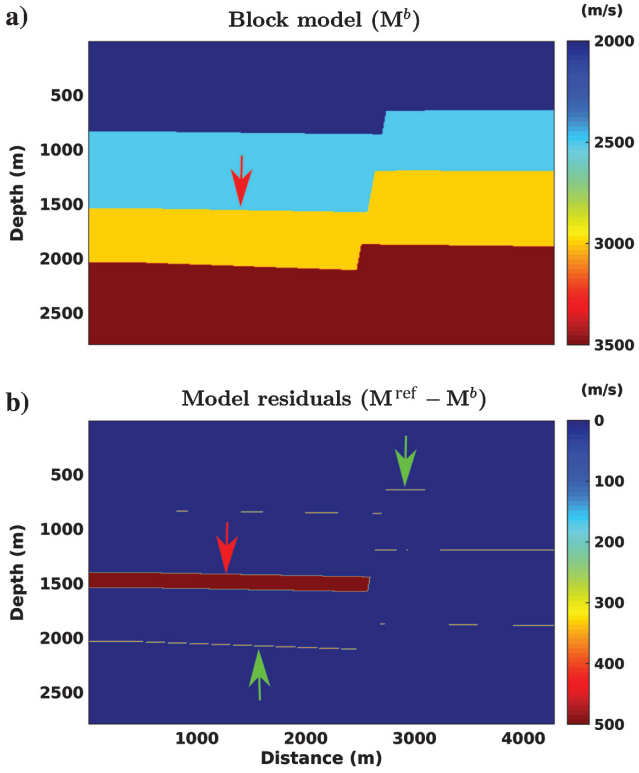


Figure 5. (a) A candidate interpretation represented as a block macrolayered velocity model ($\mathbf{M}^b$) built using the migration model in Figure 4b, as described by equation 1. The red arrow identifies the part of the horizon that was mispositioned during interpretation. (b) Model residual, difference between (a) and the reference model in Figure 4a. The red arrow identifies the interpretation error, whereas the green arrows identify picking errors.

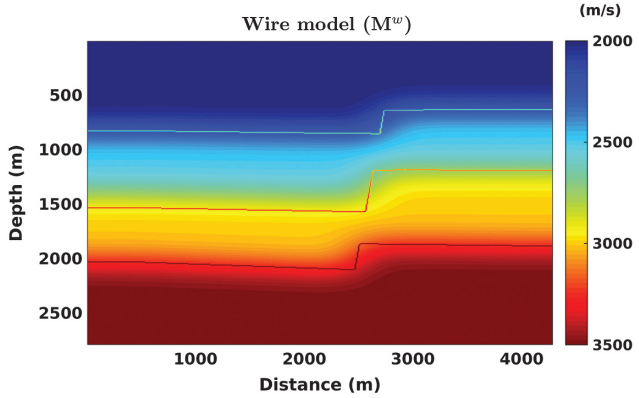


Figure 6. The same candidate interpretation from Figure 5a represented using a wire macrolayered model ($\mathbf{M}^w$), as described by equation 2.

Downloaded 03/14/19 to 138.67.129.23. Redistribution subject to SEG license or copyright; see Terms of Use at http://library.seg.org/

where $\bar{\mathbf{M}}^b$ is a smooth velocity model obtained by smoothing the slowness of $\mathbf{M}^b$. The idea behind the reflectivity macrolayered model comes from the Born approximation, which approximates the true velocity model by the sum of a smooth background model plus a reflectivity function (Bleistein et al., 2001, chapter 2); the method proposed here attempts to replace the interpretation-dependent smooth background model $\bar{\mathbf{M}}^b$ with the migration velocity model $\mathbf{M}^{\text{mig}}$.

Density macrolayered velocity models

Finally, we propose a variable density macrolayered model $\mathbf{M}^d$ given by the pair $(\mathbf{M}^{\text{mig}}, \mathbf{M}^*)$, where $\mathbf{M}^*$ is a density model estimated from $\mathbf{M}^b$, by Gardner's law, for example (Gardner et al., 1974). The variable density model allows us to propose different macrolayered velocity models that are kinematically equivalent to the migration model by proposing different impedance models.

DATA-SPACE MISFIT FUNCTIONS

Seismic data can only contain structural information about subsurface regions that have been illuminated by the wavefield recorded at receivers. Therefore, a data-misfit value computed for a given structural interpretation will only be representative of the illuminated region, and not of the entire model. Furthermore, a misfit value is a scalar, so it summarizes all the interpretation errors in the model in just one value. As a consequence, the best information that a global misfit can offer is to determine which of two models is better than the other, but not why (i.e., where the errors are coming from). This motivates the need to look for misfit functions that are localized in space, i.e., data-misfit functions that are a function of space. It is important that we know where the errors are coming from in our model because we might be able to update our structural interpretation in that region to lower the misfit. With this in mind, we propose a data-misfit function of the form

$$\Phi_i^d(\Omega) = \sum_{\mathbf{s},\mathbf{r}} \sum_{\mathbf{x}\in\Omega} \omega(\mathbf{s},\mathbf{r},\mathbf{x}) \chi[f_o(\mathbf{s},\mathbf{r},t), f_i(\mathbf{s},\mathbf{r},t)], \quad (4)$$

where Ω is the region in the model that we would like to evaluate, ω is a weighting function depending on the illumination in Ω, $f_o(\mathbf{s},\mathbf{r})$ is an observed seismogram from a shot fired at $\mathbf{x}_s = \mathbf{s}$ and recorded at a receiver at $\mathbf{x}_r = \mathbf{r}$, $f_i(\mathbf{s},\mathbf{r})$ is the corresponding synthetic seismogram computed in the candidate macrolayered velocity model $\mathbf{M}_i$, and χ is a data residual function computing the mismatch between the observed and synthetic data. We will consider one region of interest Ω at a time; this region can have an arbitrary shape, provided it is illuminated by at least one source-receiver raypath. The data-misfit 4 can be written in the more compact form

$$\Phi_i^d(\Omega) = \sum_{\mathbf{x}\in\Omega} \mathbf{W}[\chi[f_o(\mathbf{s},\mathbf{r},t), f_i(\mathbf{s},\mathbf{r},t)]], \quad (5)$$

where it is now more apparent that the data-misfit function 5 acts in two steps: first, the residual function χ maps the data plane $\mathbb{D}\times\mathbb{D}$ to a reduced data-space $\mathbb{D}'$; second, the weighting operator $\mathbf{W}$ maps the reduced data-space $\mathbb{D}'$ to the image-space $\mathbb{I}$. Here, the image space refers to the range of any seismic imaging operator; it is usually referred to as the image domain. The reduced data space is, by definition, the range of the residual function χ; a concrete example of a reduced data space will be presented in the following paragraph. Therefore, if we can find an appropriate linear relation $\mathbf{L}$ that maps $\mathbb{I}$ to $\mathbb{D}'$, the weight function ω can be determined from $\mathbf{L}^*:\mathbb{D}'\to\mathbb{I}$, where $\mathbf{L}^* = \mathbf{W}$ is either the adjoint or the pseudoinverse of $\mathbf{L}$. In this paper, we limit ourselves to the case in which $\mathbf{L}^*$ is the adjoint and we defer the possibility of $\mathbf{L}^*$ being the pseudoinverse for further investigations. In summary, we propose the following steps for using the localized data-misfit function 5 defined above:

- Find an appropriate residual function $\chi:\mathbb{D}\times\mathbb{D}\to\mathbb{D}'$.
- Find an appropriate linear map $\mathbf{L}:\mathbb{I}\to\mathbb{D}'$.
- Find the adjoint $\mathbf{L}^*:\mathbb{D}'\to\mathbb{I}$.
- Determine the weight function ω from $\mathbf{L}^* = \mathbf{W}$.

Example for vertical seismic profiling data

A common choice of $\chi:\mathbb{D}\times\mathbb{D}\to\mathbb{D}'$ for VSP data is the L^2-norm of data windowed around the first-arrival pick (Pratt and Shipp, 1999):

$$\chi[f_o(\mathbf{s},\mathbf{r},t), f_i(\mathbf{s},\mathbf{r},t)] = \sum_{t=\tau(\mathbf{s},\mathbf{r})+\Delta t}^{t=\tau(\mathbf{s},\mathbf{r})-\Delta t} [f_o(\mathbf{s},\mathbf{r},t) - f_i(\mathbf{s},\mathbf{r},t)]^2 = f(\mathbf{s},\mathbf{r}), \quad (6)$$

where $\tau(\mathbf{s},\mathbf{r})$ is the traveltime from $\mathbf{s}$ to $\mathbf{r}$, and Δt is half the time-window size. In this case, an object in the reduced data space $\mathbb{D}'$ is a function of the source and receiver coordinates $(\mathbf{s},\mathbf{r})$; therefore, we need to look for $\mathbf{L}:f(\mathbf{x})\to f(\mathbf{s},\mathbf{r})$. Let us choose $\mathbf{L}$ to be the integration of traveltime along a ray from the source to the receiver:

$$\mathbf{L}[m(\mathbf{x})] = \sum_{\mathbf{x}} dl(\mathbf{s},\mathbf{r},\mathbf{x})[m(\mathbf{x})] = \tau(\mathbf{s},\mathbf{r}), \quad (7)$$

where $dl(\mathbf{s},\mathbf{r},\mathbf{x})$ is a ray-segment centered at $\mathbf{x}$ along the ray and $m(\mathbf{x})$ is the slowness model at $\mathbf{x}$. The adjoint $\mathbf{L}^*$ is readily available (e.g., Christensen, 2010, chapter 4):

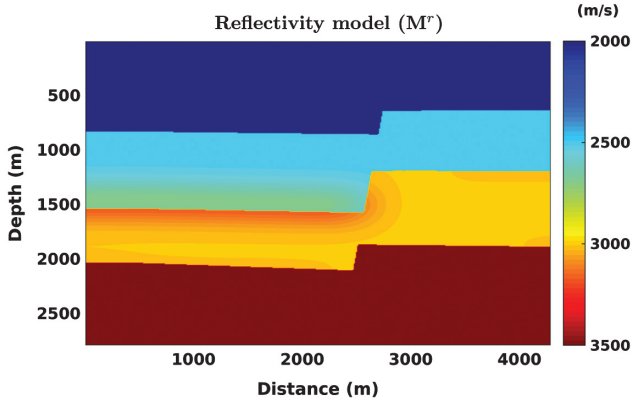


Figure 7. The same candidate interpretation from Figure 5a represented using a reflectivity macrolayered model ($\mathbf{M}^r$), as described by equation 3.

Downloaded 03/14/19 to 138.67.129.23. Redistribution subject to SEG license or copyright; see Terms of Use at http://library.seg.org/

$$\begin{aligned}\langle \mathbf{L}[f(\mathbf{x})], f(\mathbf{s},\mathbf{r})\rangle_{\mathbb{D}'} &= \sum_{\mathbf{s},\mathbf{r}}\left(\sum_{\mathbf{x}} dl(\mathbf{s},\mathbf{r},\mathbf{x}) f(\mathbf{x})\right) f(\mathbf{s},\mathbf{r}),\\ &= \sum_{\mathbf{x}} f(\mathbf{x})\left(\sum_{\mathbf{s},\mathbf{r}} dl(\mathbf{s},\mathbf{r},\mathbf{x}) f(\mathbf{s},\mathbf{r})\right),\\ &= \langle f(\mathbf{x}), \mathbf{L}^*[f(\mathbf{s},\mathbf{r})]\rangle_{\mathbb{I}}, \end{aligned} \tag{8}$$

where $<\cdot,\cdot>_{\mathbb{I}}$ denotes an inner product defined in $\mathbb{I}$. By comparing $\mathbf{L}^*$ as defined in equation 8 to equation 4, we can identify $\omega(\mathbf{s},\mathbf{r},\mathbf{x}) = dl(\mathbf{s},\mathbf{r},\mathbf{x})$. Because the rays can always be interpolated such that all ray-segments $dl(\mathbf{s},\mathbf{r},\mathbf{x}) = 1$, we conclude that

$$w(\mathbf{s},\mathbf{r},\mathbf{x}) = \begin{vmatrix} 1 & \text{if } \mathbf{x} \text{ is along the ray connecting } \mathbf{s} \text{ and } \mathbf{r},\\ 0 & \text{otherwise.}\end{vmatrix} \tag{9}$$

This implies that, for VSP, we can also rewrite the data-misfit 4 as

$$\Phi_i^d(\Omega) = \sum_{\mathbf{s},\mathbf{r}} \omega(\mathbf{s},\mathbf{r},\Omega)\chi[f_o(\mathbf{s},\mathbf{r},t), f_i(\mathbf{s},\mathbf{r},t)], \tag{10}$$

where $\omega(\mathbf{s},\mathbf{r},\Omega)$ is the length of the ray segment that actually goes through Ω.

The cartoon in Figure 8 shows the geometrical interpretation of using the data misfit 4 along with equations 6 and 9. The data misfit is projecting data residuals along rays that illuminate the region of interest Ω; this projection (of data residuals into the image space) is equivalent to a generalized Radon transform back-projection (e.g., Toft, 1996, chapter 4). Figure 8a shows rays emanating from sources at the free surface to receivers in a well. The green raypaths illuminate the region of interest Ω, whereas the black raypaths do not; only the green raypaths will actually contribute to the data-misfit 4. However, the data misfit is still not localized enough: Errors are projected along entire rays because every point $\mathbf{x}$ along the green rays has $\omega(\mathbf{s},\mathbf{r},\mathbf{x}) = 1$, according to equation 9. Therefore, for χ and ω as given by equations 6 and 9, respectively, it is impossible to limit the contribution of the data misfit 4 to points $\mathbf{x} \in \Omega$ in the most general case. This is a violation of condition 6. Figure 8b shows how we can localize the misfit better by adding an additional well to illuminate the region of interest from a different direction. In this case, points $\mathbf{x}$ along the green rays have $\omega(\mathbf{s},\mathbf{r},\mathbf{x}) = 2$ if $\mathbf{x} \in \Omega$ (i.e., where the two family of raypaths cross each other); otherwise, $\omega(\mathbf{s},\mathbf{r},\mathbf{x}) = 1$.

Example for surface seismic data

A common choice of $\chi: \mathbb{D}\times\mathbb{D} \to \mathbb{D}'$ for surface data is the $L^p (p \in [1,2])$ difference data residuals (Engquist and Froese, 2014); i.e.,

$$\chi[f_o(\mathbf{s},\mathbf{r},t), f_i(\mathbf{s},\mathbf{r},t)] = |f_o(\mathbf{s},\mathbf{r},t) - f_i(\mathbf{s},\mathbf{r},t)|^p. \tag{11}$$

Our numerical experiments suggest that this is not the best choice of χ for appraising structural interpretations using reflection data. Consider, for example, the reference and interpreted models in Figures 4a and 5a, respectively; reflection shot gathers from each of these models are shown in Figure 9a and 9b. In Figure 5b, we distinguish interpretation errors from picking errors. Interpretation errors typically result from mispositioning geologic interfaces due to poor resolution of a seismic image, whereas picking errors result from mispositioning geologic interfaces due to the fact that it is rarely possible to manually perfectly track a reflector on a seismic image. Looking at the model-space residuals (Figure 5b), picking errors are practically negligible, whereas in the data space (Figure 9c), picking errors are as strong as interpretation errors. This is problematic because picking errors are inevitable in practice. In Figure 9c, the picking errors identified by the top green arrow are strong because of the high amplitude of early arrivals; the picking errors identified by the bottom green arrow are important because of the velocity error introduced by the interpretation error above them. This second point motivates the use of macrolayered velocity models that are kinematically equivalent to the migration velocity model when appraising structural interpretations using surface data: If a macrolayered velocity model introduces a velocity error, then all the reflectors below this error will be mispositioned in the data space even if they were positioned at the right place in the image space by the interpreter. This eventually leads to a violation of condition 6 after back-projecting data errors into the image space. An illustration of these problems is presented in Figure 10, where we compare individual traces. Figure 10a compares a trace from Figure 9a against a trace from Figure 9b; the difference between these two traces is shown in Figure 10b, where it can be noted that picking errors (δp) are as strong as errors due to mispositioning of horizons (δh). Figure 10c shows a similar experiment but using synthetic data computed in the more kinematically accurate reflectivity macrolayered model in Figure 7; in this case, the additional velocity errors are removed as highlighted by the green circle in Figure 10c.

In addition to being very sensitive to picking errors, equation 11 also suffers from cycle skipping: If a horizon's position is progressively shifted away from its true position, there is a limit beyond which a data misfit computed using equation 11 will no longer depend on the horizon's position (Engquist and Froese, 2014). This is

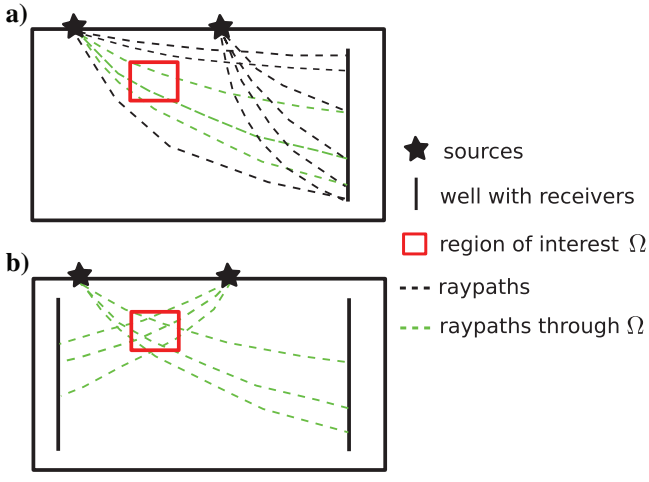


Figure 8. Geometrical interpretation of the VSP misfit weight function. (a) Receivers are positioned only in one well. The green rays correspond to source-receiver pairs that will actually contribute to the data misfit 4. According to equation 9, data-misfit values are projected along entire rays because every point $\mathbf{x}$ along the green rays has $\omega(\mathbf{s},\mathbf{r},\mathbf{x}) = 1$. (b) Receivers are positioned in two wells, thus illuminating the region of interest from different directions. Now points $\mathbf{x}$ along the green rays have $\omega(\mathbf{s},\mathbf{r},\mathbf{x}) = 2$ if $\mathbf{x} \in \Omega$; otherwise, $\omega(\mathbf{s},\mathbf{r},\mathbf{x}) = 1$.

a violation of condition 7. For instance, the data misfit $\phi_i^d(\mathbf{s},\mathbf{r}) = \sum_t \chi[f_o(\mathbf{s},\mathbf{r},t), f_i(\mathbf{s},\mathbf{r},t)]$ between the two traces in Figure 10a would not change significantly if the mispositioned horizon in Figure 5a was shifted further down because the corresponding reflection pulse no longer overlaps with the reference one. We therefore conclude that the $L^p(p \in [1,2])$ seismogram difference is not the best choice for χ. In principle, phase data residuals can overcome the aforementioned problems. Here, a phase residual refers to any function of time that measures phase shifts between two signals. Such residual functions include dynamic-warping-based techniques (Hale, 2013), and optimal-transport-based techniques (Engquist and Froese, 2014). The dynamic-time-warping (DTW) phase residual $\delta\phi(\mathbf{s},\mathbf{r},t)$ of $f_o(\mathbf{s},\mathbf{r},t)$ and $f_i(\mathbf{s},\mathbf{r},t)$ is defined as (Hale, 2013)

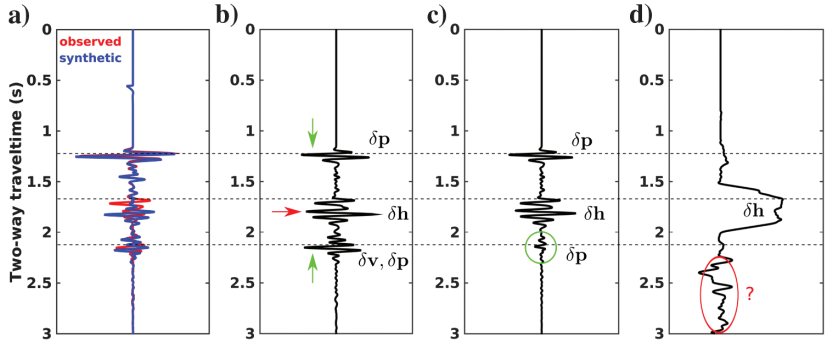


Figure 10. Data residuals of two traces from Figure 9. (a) Comparison between observed (red) against synthetic (blue) traces. (b) Difference between observed and synthetic traces. The top green arrow identifies picking errors (δp), the bottom green arrow identifies picking errors in addition to velocity errors (δv) in the macrolayered model in Figure 5a, and the red arrow identifies horizon mispositioning error (δh). (c) The same as (b) but using synthetic data from the more kinematically accurate macrolayered model in Figure 7. Velocity errors are removed as highlighted by the green circle. (d) DTW phase residual using synthetic data from the model in Figure 7.

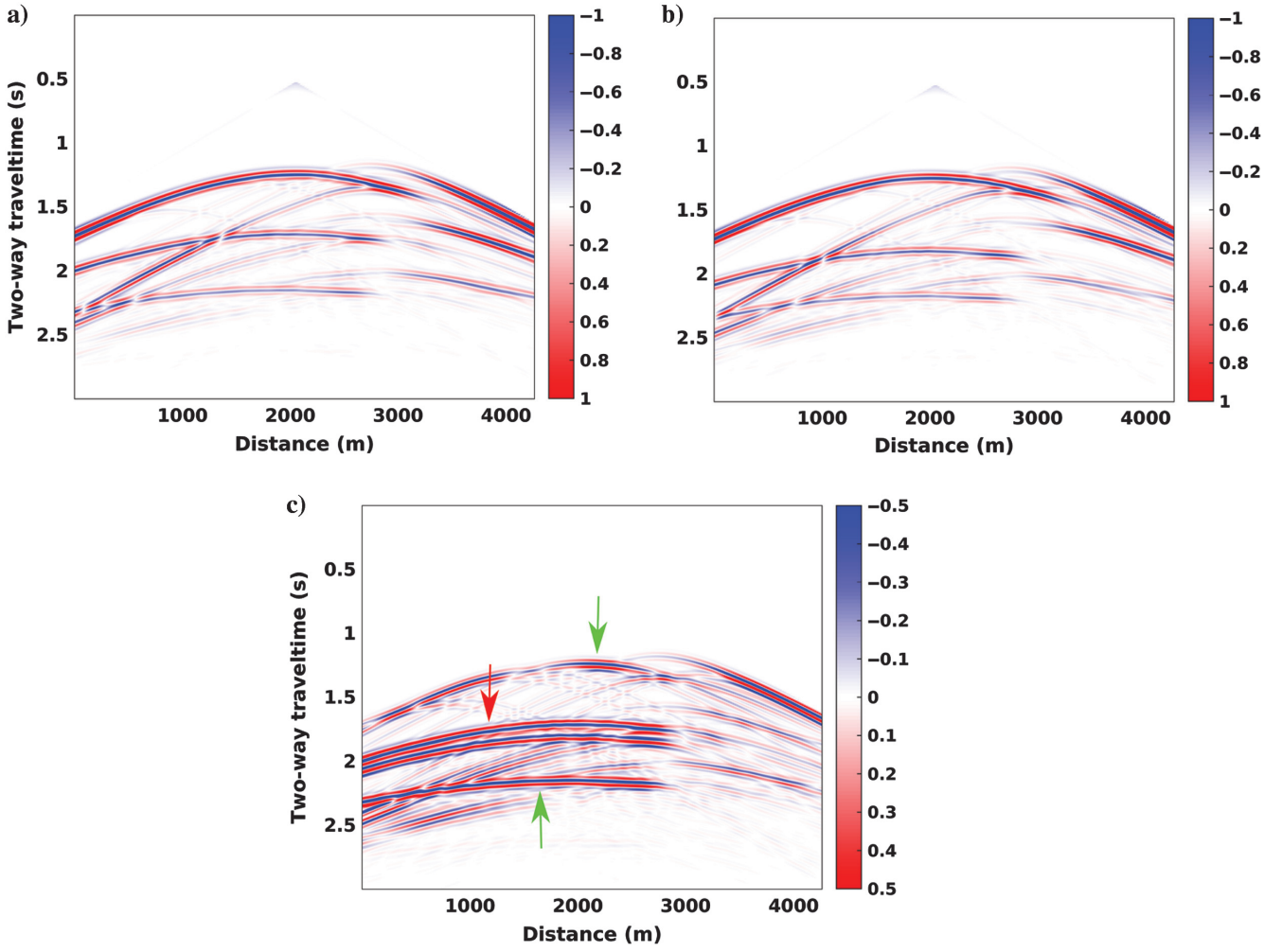


Figure 9. (a) Observed data simulated in the model of Figure 4a. (b) Synthetic data simulated in the model of Figure 5a. (c) Data residuals, the difference between the observed and synthetic data. The red arrow identifies residuals due to the interpretation error shown in Figure 5b; the green arrows identify residuals due to picking errors, also shown in Figure 5b.

Downloaded 03/14/19 to 138.67.129.23. Redistribution subject to SEG license or copyright; see Terms of Use at http://library.seg.org/

Downloaded 03/14/19 to 138.67.129.23. Redistribution subject to SEG license or copyright; see Terms of Use at http://library.seg.org/

$\delta\phi(\mathbf{s},\mathbf{r},t)$, such that

$$\sum_t |f_o(\mathbf{s},\mathbf{r},t) - f_i(\mathbf{s},\mathbf{r},t+\delta\phi(\mathbf{s},\mathbf{r},t))|^2 \text{is minimized.} \quad (12)$$

Figure 10d shows the data residuals of the two signals in Figure 10a using this choice of χ. We note that such a misfit is more sensitive to horizon mispositioning errors and it is less sensitive to picking errors. However, such a misfit can have some undesired effects as highlighted by the red ellipse. When using equation 11 or 12, an object in the reduced data space $\mathbb{D}'$ is a function of time as well as the source-and-receiver coordinates, that is $\mathbb{D}' = \mathbb{D}$; therefore, we need to look for $\mathbf{L}: f(\mathbf{x}) \rightarrow f(\mathbf{s},\mathbf{r},t)$. For simplicity, let us choose $\mathbf{L}$ to be a Kirchhoff-type modeling operator

$$\mathbf{L}[m(\mathbf{x})] = \sum_{\mathbf{x}} \alpha(\mathbf{s},\mathbf{x},\mathbf{r}) S(t-\tau(\mathbf{s},\mathbf{x},\mathbf{r}))[m(\mathbf{x})] = f(\mathbf{s},\mathbf{r},t), \quad (13)$$

where $f(\mathbf{s},\mathbf{r},t)$ is the computed trace recorded at receiver $\mathbf{r}$ from a shot at $\mathbf{s}$, $S(t)$ is the source wavelet, $\alpha(\mathbf{s},\mathbf{x},\mathbf{r})$ are "appropriate" migration weights such as may be found, for example, in Cohen et al. (1986), $\tau(\mathbf{s},\mathbf{x},\mathbf{r})$ is the traveltime for a ray originating from $\mathbf{s}$ scattered off $\mathbf{x}$ and recorded at $\mathbf{r}$, and m is the reflectivity model. The adjoint $\mathbf{L}^*$ is readily available:

$$\begin{aligned}
&\langle \mathbf{L}[f(\mathbf{x})], f(\mathbf{s},\mathbf{r},t)\rangle_{\mathbb{D}'=\mathbb{D}} \\
&= \sum_{\mathbf{s},\mathbf{r},t} \left(\sum_{\mathbf{x}} \alpha(\mathbf{s},\mathbf{x},\mathbf{r}) S(t-\tau(\mathbf{s},\mathbf{x},\mathbf{r})) \right) f(\mathbf{x})) f(\mathbf{s},\mathbf{r},t), \\
&= \sum_{\mathbf{x}} f(\mathbf{x}) \left(\sum_{\mathbf{s},\mathbf{r},t} \alpha(\mathbf{s},\mathbf{x},\mathbf{r}) S(t-\tau(\mathbf{s},\mathbf{x},\mathbf{r})) f(\mathbf{s},\mathbf{r},t) \right), \\
&= \langle f(\mathbf{x}), \mathbf{L}^*[f(\mathbf{s},\mathbf{r},t)] \rangle_{\mathbb{I}}. \quad (14)
\end{aligned}$$

$\mathbf{L}^*$ as defined in equation 14 differs from the standard KDM in that it does not have a derivative along the vertical axis. One often defines (Schneider, 1978)

$$\text{KDM}[f(\mathbf{s},\mathbf{r},t)] = \frac{\partial}{\partial z} \mathbf{L}^*[f(\mathbf{s},\mathbf{r},t)], \quad (15)$$

or (Santos et al., 2000)

$$\text{KDM}[f(\mathbf{s},\mathbf{r},t)] = \mathbf{L}^* \left[\frac{\partial}{\partial t} f(\mathbf{s},\mathbf{r},t) \right]; \quad (16)$$

we use this latter definition of KDM hereafter.

By comparing $\mathbf{L}^*$ as defined in equation 14 to equation 4, we can identify

$$\omega(\mathbf{s},\mathbf{r},\mathbf{x}) = \sum_t \alpha(\mathbf{s},\mathbf{x},\mathbf{r}) S(t-\tau(\mathbf{s},\mathbf{x},\mathbf{r})). \quad (17)$$

The interpretation of this result is that the localized data misfit 4 merely amounts to migrating data residuals for surface data. Figure 11a shows the $\mathbf{L}^*$ projection of L^1 data residuals of waveforms computed in the model in Figure 4a and waveforms computed in the model in Figure 5a; notable contributions of picking errors (green arrows) and velocity errors (red arrow) are observed. Figure 11b shows the $\mathbf{L}^*$ projection of L^1 data residuals of waveforms computed in the model in Figure 4a and waveforms computed in the model in Figure 7; velocity errors are dramatically reduced because the model in Figure 7 is more kinematically accurate than the model in Figure 5a. Figure 12a shows the KDM of DTW data residuals of waveforms computed in the model in Figure 4a and waveforms computed in the model in Figure 7. We observe that high-frequency noise is present and that the residual map has two poles: a positive contribution above the black line and a negative contribution below the black line. The high-frequency noise and the bipolarity of projected residuals are a footprint of the derivative along the vertical axis in KDM, and they can be removed by using the $\mathbf{L}^*$ projection as shown in Figure 12b.

APPLICATION AND DISCUSSION

Appraising structural interpretations quantitatively is a challenging problem. Consider the eight different structural models in Figure 13 interpreted from the seismic image in Figure 2b by different interpreters. We would like to rank those structural models using VSP data from the most likely to the least likely. For each structural model, we built a block macrolayered velocity model, allowing us to compute VSP synthetic data for each structural model. Observed VSP data were generated in the reference model in Figure 1, with

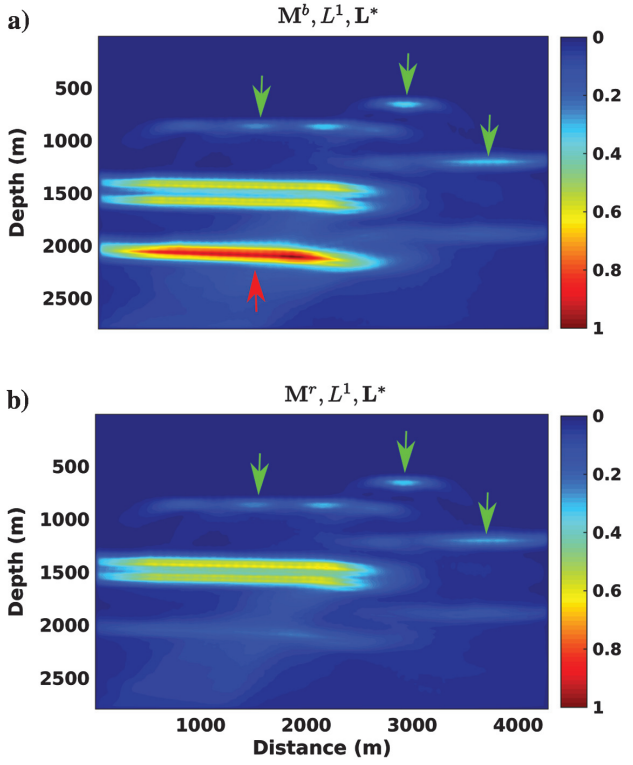


Figure 11. (a) Projection of L^1 data residuals (equation 11, with $p = 1$) into the image space using $\mathbf{L}^*$ (defined in equation 14). Synthetic data were computed in the macrolayered model in Figure 5a. Green arrows identify picking errors, whereas the red arrow identifies velocity errors. (b) Projection of L^1 data residuals into the image space using $\mathbf{L}^*$. Synthetic data were computed in the more accurate macrolayered model in Figure 7. The effect of velocity errors is removed.

Downloaded 03/14/19 to 138.67.129.23. Redistribution subject to SEG license or copyright; see Terms of Use at http://library.seg.org/

sources covering the free surface and receivers positioned in a vertical well at $x = 7500$ m. First, we tried to rank the structural models using a data misfit defined as the L^1-norm of the entire data set, for each model. Figure 14a shows that the data-space ranking obtained this way is not consistent with the ranking expected in the model space (the model-space misfits were computed as the L^1-norm of block macrolayered velocity models and the reference velocity model). We then tried to rank the structural models using the method proposed in this paper. Figure 14b shows the results

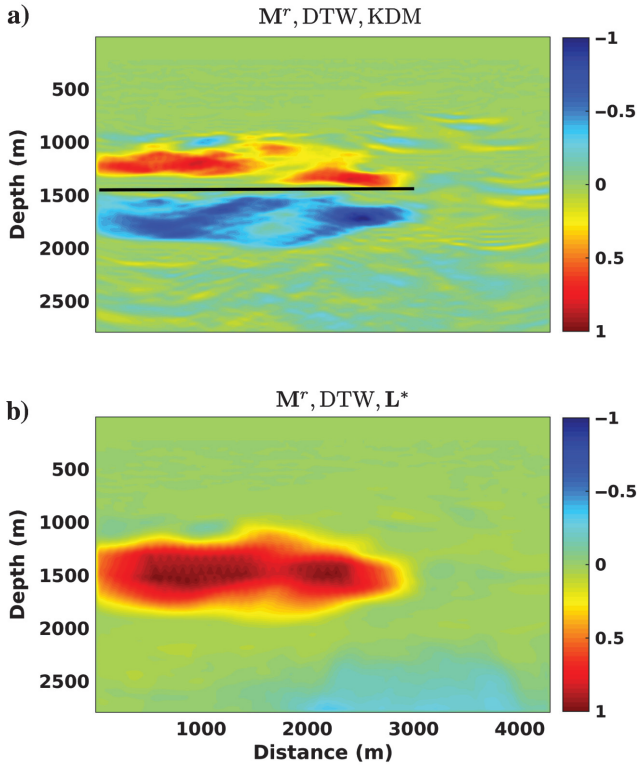


Figure 12. (a) Projection of DTW data residuals (equation 12) into the image space using KDM (defined in equation 16). Synthetic data were computed in the macrolayered model in Figure 7. The black line highlights the bipolarity of the residuals by separating positive residuals above from negative residuals below. (b) Projection of DTW data residuals into the image-space using $\mathbf{L}^*$ (defined in equation 14). Synthetic data were computed in the macrolayered model in Figure 7.

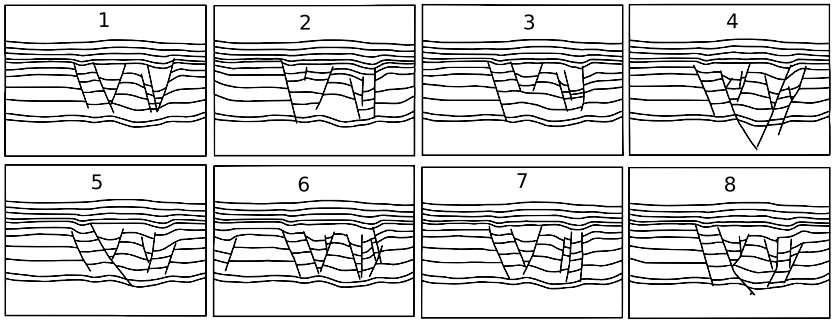


Figure 13. Eight possible structural interpretations/models of the seismic image in Figure 2b from different interpreters.

obtained by limiting the model-misfit and the data misfit to the region of interest, i.e., the black box in Figure 2b, and by relying on equations 4, 6, and 9 to define the data misfit. We observe that the scatterplot in Figure 14b satisfies condition 8, whereas the scatterplot in Figure 14a does not. The model-misfit axis in Figure 14a and 14b shows that model 1 is the best model. The data misfit in Figure 14b was able to indentify model 1 as the best model, whereas the data misfit in Figure 14a identified model 3 as the best model. In fact, the data misfit in Figure 14b was able to successfully rank all the models except model 7.

The present paper focuses on misfit functions with the aim of determining the possible reasons as to why the straightforward approach implemented in Figure 14a fails. First, we argue that one should use localized data misfits $\Phi^d(\Omega)$. It follows that conditions 6 and 7 are necessary conditions for being able to rank structural models using $\Phi^d(\Omega)$, if we expect data-space ranking to be consistent with model-space ranking. These conditions are expected to be valid if the available candidate structural models are "close enough" to the (unknown) reference model. Condition 6 mandates that a perturbation of the data-misfit value $\Phi_i^d(\Omega)$ in the region Ω of the ith model should only occur if that model is modified in that specific region Ω. Condition 7 mandates that if the ith model is modified in the region Ω, the data misfit $\Phi_i^d(\Omega)$ corresponding to that region should change as well.

For VSP data, condition 7 can readily be satisfied by computing Φ^d using only source-receiver pairs that illuminate Ω (e.g., using equation 9) and windowing data, along the time axis, around the first arrival (e.g., using equation 6). The difficulty then comes from satisfying condition 6, which is impossible in the most general case as any perturbation of the structural model at any point along any raypath through Ω will lead to a perturbation of Φ^d, not just points in Ω. This difficulty can be alleviated, in principle, by adding data that illuminate Ω from different directions as illustrated in Figure 8.

For surface seismic data, using $L^p(p \in [1,2])$ data residuals, we show that velocity errors introduced in macrolayered velocity models can lead to a perturbation of $\Phi^d(\Omega)$ for a region Ω below the velocity error even in the absence of any structural interpretation errors in Ω (Figure 11a), thereby violating condition 6. We also argue that if a reflector in the structural model is shifted away from its true position until its reflection pulse no longer overlaps with true reflection-pulse along the time axis, shifting the reflector further in the model would not necessarily affect the data misfit, thereby violating condition 7. However, it is possible, in principle, to approximate condition 7 by using more appropriate data residuals, such as phase-shift residuals. The challenge then becomes how to compute phase shifts for complex data sets; this is a subject of ongoing investigations.

The proposed method assumes that the region of interest is well illuminated. We can therefore expect the method to perform poorly for more challenging seismic imaging targets, such as subsalt areas for example. Moreover, appraising structural models using surface seismic data requires a kinematically accurate migration velocity model, which is not easy to obtain in practice. Challenging our approach with a realistic migration velocity model obtained by migration velocity analysis is a subject of ongoing investigations.

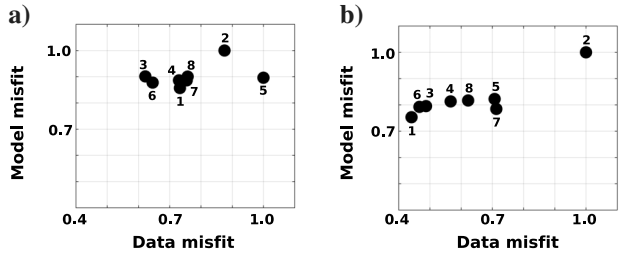


Figure 14. Appraising the structural models in Figure 13 using VSP data. Each point represents a structural model from Figure 13. The observed data were computed in the reference model in Figure 1, with sources positioned at the free surface and receivers positioned in a vertical well at $x = 7500$ m. (a) The data-space ranking obtained using the L^1-norm of the entire data set is not consistent with the ranking expected in the model-space. (b) The data-space ranking obtained using the localized data misfit 4, along with equations 6 and 9, is consistent with the ranking expected in the model space. The region of interest Ω is the black box in Figure 2b.

CONCLUSION

In this paper, we propose a theoretical formulation and some general solutions to the problem of appraising structural interpretations using seismic data. Assuming that the different structural models are close to the unknown true model, we propose a set of conditions imposed on data-space misfit functions needed for a reliable model appraisal. We argue that misfit functions should be able to localize interpretation errors in the image space. This localization of errors is achieved by back-projection of data residuals into the image space. It follows that, because it is not possible to truly localize errors using VSP data, one cannot predict which interpretations are more probable than others using VSP data in the most general case. However, it is expected that VSP data can always be used to statistically rank structural interpretations if the data illuminate the target from different directions. As for appraising structural models using surface seismic data, we expect a better localization of errors, compared with VSP, and therefore a better chance for ranking structural interpretations. The challenge when using surface seismic data is to define appropriate data residual functions. We argue that phase-shift residual functions, such as dynamic-warping and optimal-transport residuals, are good candidates; our current work involves finding robust ways to compute such phase-shift residuals for data acquired in complex geologic settings.

ACKNOWLEDGMENTS

The authors would like to thank L. Métivier and P. Thore for fruitful discussions about the subject. This work also greatly benefited from constructive discussions with T. Bodin and Y. Capdeville in the frame of the HIWAI Project. We are very thankful to E. L'Heureux, I. Lecomte, S. Davis, and X. Wu for the time they dedicated to review this paper. We would also like to thank C. Butault, F. Bonneau, and P. Angrand, for some seismic interpretations used in this work. The traveltime maps needed to evaluate Kirchhoff integral operators were computed using the Madagascar software freely available from www.ahay.org. This work was done in the frame of the RING project at the Université de Lorraine. The sponsors of the RING-GOCAD Consortium managed by ASGA are hereby acknowledged for their support. We would also like to thank Paradigm for providing the SKUA-GOCAD software used for structural modeling.

DATA AND MATERIALS AVAILABILITY

Data associated with this research are available and can be obtained by contacting the corresponding author.

REFERENCES

Abrahamsen, P., 1993, Bayesian kriging for seismic depth conversion of a multi-layer reservoir: Geostatistics Troia, **92**, 385–398.
Alcalde, J., C. Bond, G. Johnson, J. Ellis, and R. Butler, 2017, Impact of seismic image quality on fault interpretation uncertainty: GSA Today, **27**, 4–10.
Beylkin, G., M. Oristaglio, and D. Miller, 1985, Spatial resolution of migration algorithms: Acoustical Imaging, **14**, 155–168.
Bleistein, N., J. W. Stockwell, and J. K. Cohen, 2001, Mathematics of multidimensional seismic imaging, migration, and inversion: Springer.
Bond, C., 2015, Uncertainty in structural interpretation: Lessons to be learnt: Journal of Structural Geology, **74**, 185–200, doi: 10.1016/j.jsg.2015.03.003.
Bond, C., Z. Shipton, and S. Jones, 2007, What do you think this is? Conceptual uncertainty in geoscience interpretation: GSA Today, **17**, 4–10, doi: 10.1130/GSAT01711A.1.
Bube, K., J. Kane, T. Nemeth, D. Medwede, and O. Mikhailov, 2004, The influence of stacking velocity uncertainties on structural uncertainties: 74th Annual International Meeting, SEG, Expanded Abstracts, 2188–2191, doi: 10.1190/1.1851209.
Caumon, G., P. Collon-Drouaillet, C. Le Carlier de Veslud, S. Viseur, and J. Sausse, 2009, Surface-based 3D modeling of geological structures: Mathematical Geosciences, **41**, 927–945, doi: 10.1007/s11004-009-9244-2.
Cherpeau, N., and G. Caumon, 2015, Stochastic structural modeling in sparse data situations: Petroleum Geoscience, **21**, 233–247, doi: 10.1144/petgeo2013-030.
Cherpeau, N., G. Caumon, J. Caers, and B. Lévy, 2012, Method for stochastic inverse modeling of fault geometry and connectivity using flow data: Mathematical Geosciences, **44**, 147–168, doi: 10.1007/s11004-012-9389-2.
Christensen, O., 2010, Functions, spaces, and expansions: Mathematical tools in physics and engineering: Birkhauser Basel.
Cohen, J., F. Hagin, and N. Bleistein, 1986, Three-dimensional Born inversion with an arbitrary reference: Geophysics, **51**, 1552–1558, doi: 10.1190/1.1442205.
Colletta, B., J. Letouzey, R. Pinedo, J. F. Ballard, and P. Balé, 1991, Computerized X-ray tomography analysis of sandbox models: Examples of thin-skinned thrust systems: Geology, **19**, 1063–1067, doi: 10.1130/0091-7613(1991)019<1063:CXRTAO>2.3.CO;2.
Collino, F., and C. Tsogka, 2001, Application of the perfectly matched absorbing layer model to the linear elastodynamic problem in anisotropic heterogeneous media: Geophysics, **66**, 294–307, doi: 10.1190/1.1444908.
Engquist, B., and B. Froese, 2014, Application of the Wasserstein metric to seismic signals: Communications in Mathematical Sciences, **12**, 979–988, doi: 10.4310/CMS.2014.v12.n5.a7.
Etgen, J., S. Gray, and Y. Zhang, 2009, An overview of depth migration in exploration geophysics: Geophysics, **74**, no. 6, WCA5–WCA17, doi: 10.1190/1.3223188.
Fomel, S., and E. Landa, 2014, Structural uncertainty of time-migrated seismic images: Journal of Applied Geophysics, **101**, 27–30, doi: 10.1016/j.jappgeo.2013.11.010.
Foss, S.-K., M. Rhodes, B. Dalstrom, C. Gram, and A. Welbon, 2008, Geologically constrained seismic imaging-workflow: Geophysics, **73**, no. 5, VE313–VE319, doi: 10.1190/1.2967500.
Fullagar, P., G. Pears, and B. McMonnies, 2008, Constrained inversion of geologic surfaces-pushing the boundaries: The Leading Edge, **27**, 98–105, doi: 10.1190/1.2831686.
Gardner, G., L. Gardner, and A. Gregory, 1974, Formation velocity and density: The diagnostic basics for stratigraphic traps: Geophysics, **39**, 770–780, doi: 10.1190/1.1440465.
Hajnal, Z., and I. Sereda, 1981, Maximum uncertainty of interval velocity estimates: Geophysics, **46**, 1543–1547, doi: 10.1190/1.1441160.
Hale, D., 2013, Dynamic warping of seismic images: Geophysics, **78**, no. 2, S105–S115, doi: 10.1190/geo2012-0327.1.
Holden, L., P. Mostad, B. F. Nielsen, J. Gjerde, C. Townsend, and S. Ottesen, 2003, Stochastic structural modeling: Mathematical Geology, **35**, 899–914, doi: 10.1023/B:MATG.0000011584.51162.69.
Hoyes, J., and T. Cheret, 2011, A review of global interpretation methods for automated 3D horizon picking: The Leading Edge, **30**, 38–47, doi: 10.1190/1.3535431.

Downloaded 03/14/19 to 138.67.129.23. Redistribution subject to SEG license or copyright; see Terms of Use at http://library.seg.org/

Julio, C., G. Caumon, and M. Ford, 2015, Sampling uncertainty about segmented normal fault interpretation using a stochastic downscaling method: Tectonophysics, **639**, 56–67, doi: 10.1016/j.tecto.2014.11.013.
Lallier, F., G. Caumon, J. Borgomano, S. Viseur, F. Fournier, C. Antoine, and T. Gentilhomme, 2012, Relevance of the stochastic stratigraphic well correlation approach for the study of complex carbonate settings: Application to the Malampaya buildup (offshore Palawan, Philippines): Geological Society of London, Special Publications, 265–275.
Landa, E., and P. Thore, 2007, Realistic finite differences modeling: A case study: 69th Annual International Conference and Exhibition, EAGE, Extended Abstracts, doi: 10.3997/2214-4609.201401548.
Lecomte, I., H. Gjoystdal, and A. Drottning, 2003, Simulated prestack local imaging: A robust and efficient interpretation tool to control illumination, resolution, and time-lapse properties of reservoirs: 73rd Annual International Meeting, SEG, Expanded Abstracts, 1525–1528, doi: 10.1190/1.1817585.
Lecomte, I., P. Lavadera, C. Botter, I. Anell, S. Buckley, C. Eide, A. Grippa, V. Mascolo, and S. Kjoberg, 2016, 2(3)D convolution modeling of complex geological targets: Beyond 1D convolution: First Break, **34**, 99–107.
Lecour, M., R. Cognot, I. Duvinage, P. Thore, and J.-C. Dulac, 2001, Modeling of stochastic faults and fault networks in a structural uncertainty study: Petroleum Geoscience, **7**, S31–S42, doi: 10.1144/petgeo.7.S.S31.
Li, L., J. Caers, and P. Sava, 2015, Assessing seismic uncertainty via geostatistical velocity model perturbation and image registration: An application to subsalt imaging: The Leading Edge, **34**, 1064–1070, doi: 10.1190/tle34091064.1.
Messud, J., M. Reinier, H. Prigent, P. Guillaume, T. Coléou, and S. Masclet, 2017, Extracting seismic uncertainties from tomographic velocity inversion and their use in reservoir analysis: The Leading Edge, **36**, 127–132, doi: 10.1190/tle36020127.1.
Pauget, F., S. Lacaze, and T. Valding, 2009, A global approach in seismic interpretation based on cost function minimization: 79th Annual International Meeting, SEG, Expanded Abstracts, 2592–2596, doi: 10.1190/1.3255384.
Pon, S., and L. R. Lines, 2005, Sensitivity analysis of seismic depth migrations: Geophysics, **70**, no. 2, S39–S42, doi: 10.1190/1.1897036.
Pratt, G., and R. Shipp, 1999, Seismic waveform inversion in the frequency domain. Part II: Fault delineation in sediments using crosshole data: Geophysics, **64**, 902–914, doi: 10.1190/1.1444598.
Santos, L., J. Schleicher, M. Tygel, and P. Hubral, 2000, Seismic modeling by demigration: Geophysics, **65**, 1281–1289, doi: 10.1190/1.1444819.
Schneider, W., 1978, Integral formulation for migration in two and three dimensions: Geophysics, **43**, 49–76, doi: 10.1190/1.1440828.
Stark, T., 2004, Relative geologic time (age) volumes-relating every seismic sample to a geologically reasonable horizon: The Leading Edge, **23**, 928–932, doi: 10.1190/1.1803505.
Suzuki, S., J. Caers, and G. Caumon, 2008, Dynamic data integration for structural modeling: Model screening approach using a distance-based model parameterization: Computational Geosciences, **12**, 105–119, doi: 10.1007/s10596-007-9063-9.
Thore, P., and A. Haas, 1996, A practical formulation of migration errors due velocity uncertainties: 58th Annual International Conference and Exhibition, EAGE, Extended Abstracts, doi: 10.3997/2214-4609.201408940.
Thore, P., A. Shtuka, M. Lecour, T. Ait-Ettajer, and R. Cognot, 2002, Structural uncertainties: Determination, management, and applications: Geophysics, **67**, 840–852, doi: 10.1190/1.1484528.
Toft, P., 1996, The radon transform: Theory and implementation: Ph.D. thesis, Technical University of Denmark.
Virieux, J., 1984, SH-wave propagation in heterogeneous media: Velocity-stress finite-difference method: Geophysics, **49**, 1933–1942, doi: 10.1190/1.1441605.
Wellmann, J., F. G. Horowitz, E. Schill, and K. Regenauer-Lieb, 2010, Towards incorporating uncertainty of structural data in 3D geological inversion: Tectonophysics, **490**, 141–151, doi: 10.1016/j.tecto.2010.04.022.
Wellmann, J., M. Lindsay, J. Poh, and M. Jessell, 2014, Validating 3-D structural models with geological knowledge for improved uncertainty evaluations: Energy Procedia, **59**, 374–381, doi: 10.1016/j.egypro.2014.10.391.
Wu, X., 2017, Building 3D subsurface models conforming to seismic structural and stratigraphic features: Geophysics, **82**, no. 3, IM21–IM30, doi: 10.1190/geo2016-0255.1.
Wu, X., and D. Hale, 2015, Horizon volumes with interpreted constraints: Geophysics, **80**, no. 2, IM21–IM33, doi: 10.1190/geo2014-0212.1.

Downloaded 03/14/19 to 138.67.129.23. Redistribution subject to SEG license or copyright; see Terms of Use at http://library.seg.org/